Monthly Notices of the ROYAL ASTRONOMICAL SOCIETY

MNRAS **541,** 3534–3548 (2025) https://doi.org/10.1093/mnras/staf1125
Advance Access publication 2025 July 11

JWST MIRI/MRS observations of hot molecular gas in an AGN host galaxy at Cosmic Noon

D. Kakkad [1,2★] V. Mainieri,[3] Takumi S. Tanaka [4,5,6] John D. Silverman,[4,5,6,7] D. Law,[2] Rogemar A. Riffel [8] C. Circosta,[9,10] E. Bertola,[11] M. Bianchin [12] M. Bischetti,[13,14] G. Calistro Rivera,[15] S. Carniani [16] C. Cicone [17] G. Cresci,[18] T. Costa [19] C. M. Harrison [19] I. Lamperti [18,20] B. Kalita,[21,22,23] Anton M. Koekemoer [2] A. Marconi,[18,20] M. Perna,[24] E. Piconcelli,[25] A. Puglisi [26] Gabriele S. Ilha [3,27] G. Tozzi,[28] G. Vietri,[29] C. Vignali,[30,31] S. Ward,[32] G. Zamorani[31] and L. Zappacosta[25]

Affiliations are listed at the end of the paper

Accepted 2025 July 4. Received 2025 July 2; in original form 2025 March 11

ABSTRACT

Active Galactic Nuclei (AGN) are believed to play a central role in quenching star formation by removing or destroying molecular gas from host galaxies via radiation-pressure driven outflows and/or radio jets. Some studies of cold molecular gas in galaxies at Cosmic Noon ($z \sim 2$) show that AGN have less cold gas (<100 K) compared to mass-matched star-forming galaxies. However, cold gas could also be shock-heated to warmer phases, detectable via H_2 transitions in the rest-frame near- and mid-infrared spectra. The Medium Resolution Spectrograph (MRS) of the Mid-infrared Instrument (MIRI) aboard *JWST* has opened a unique window to observe these emission lines in galaxies at Cosmic Noon. We present the first detection of hot molecular gas in cid_346, an X-ray AGN at $z \sim 2.2$, via the H_2 ro-vibrational transition at 2.12 μm. We measure a hot molecular gas mass of $\sim 8.0 \times 10^5$ $M_\odot$, which is $\sim 10^5 - 10^6$ times lower than the cold molecular gas mass. cid_346 is located in an environment with extended gas structures and satellite galaxies. This is supported by detection of hot and cold molecular gas out to distances >10 kpc in MIRI/MRS and ALMA data, respectively and ancillary NIRCam imaging that reveals two satellite galaxies at distances of ∼0.4 arcsec (3.3 kpc) and ∼0.9 arcsec (7.4 kpc) from the AGN. Our results tentatively indicate that while the CO(3-2)-based cold gas phase dominates the molecular gas mass at Cosmic Noon, H_2 ro-vibrational transitions are effective in tracing hot molecular gas locally in regions that may lack CO emission.

Key words: techniques: spectroscopic – methods: observational – galaxies: active – galaxies: individual – (galaxies:) quasars: supermassive black holes.

1 INTRODUCTION

Feedback from growing supermassive black holes, also known as Active Galactic Nuclei (AGN), has become a fundamental component of cosmological simulations that model galaxy formation and evolution (e.g. Genel et al. 2014; Hirschmann et al. 2014; Schaye et al. 2015; Dubois et al. 2016; Pillepich et al. 2018; Schaye et al. 2023). AGN feedback plays a key role in limiting star formation efficiency, particularly in galaxies with high halo masses (e.g. Benson et al. 2003; Somerville et al. 2008; Harrison 2017; Rennehan et al. 2024). As a result of incorporating these feedback mechanisms, simulations now closely match the observed stellar mass functions of galaxies, especially at low redshifts (see also Silk & Mamon 2012).

Observations of multiphase gas outflows have been crucial in identifying signatures of ongoing AGN-driven feedback. Numerous studies, ranging from fibre or slit spectroscopy to integral field spectroscopy (IFS) in rest-frame optical wavelengths, have successfully detected fast winds (velocity, $v > 1000\,\mathrm{km\,s^{-1}}$) in the ionized gas phase of AGN, star-forming, and starburst galaxies. These studies often use [O III]λ5007 ([O III]hereafter) or H α as ionized gas tracers, covering galaxies from low-redshift to Cosmic Noon ($1 < z < 3$) to the Epoch of Reionization (e.g. Arribas et al. 2014; Harrison et al. 2014; Förster Schreiber et al. 2018; Rakshit & Woo 2018; Davies et al. 2020; Kakkad et al. 2022, 2023a; Carniani et al. 2023; Loiacono et al. 2024; Roy et al. 2024; Tozzi et al. 2024; Travascio et al. 2024; Vayner et al. 2024). Outflows have also been observed in the molecular gas phase, where they are believed to carry the bulk of the outflow mass in galaxies (e.g. Cicone et al. 2014; Carniani et al. 2015; Fiore et al. 2017; Fluetsch et al. 2019; Lutz et al. 2020; Veilleux et al. 2020). These outflows are expected to be especially important in delivering feedback into the interstellar medium (ISM) during Cosmic Noon, when both the volume-averaged star formation rate (SFR) and AGN accretion activity reach their peak (e.g. Shankar, Weinberg & Miralda-Escudé 2009; Madau & Dickinson 2014).

★ E-mail: darshankakkad@gmail.com

The relationship between AGN activity and star formation, particularly the impact of AGN-driven outflows on SFR, remains a topic of active debate in the literature. AGN activity is typically identified by excess emission in various wavelengths – beyond what can be attributed to star formation or internal processes within the host galaxy – such as hard X-rays, mid-infrared, or radio, as well as through nebular diagnostics in UV, optical, or infrared wavelengths (e.g. Baldwin, Phillips & Terlevich 1981; Hirschmann et al. 2023). The time-scales of this AGN activity can differ by several orders of magnitude ($> 10^5$ yr: Schawinski et al. 2015; Padovani et al. 2017). SFR, on the other hand, is conventionally measured using short-term tracers ($\sim$10 Myr) like Hα or [O II]λ3727 emission lines (e.g. Glazebrook et al. 1999; Murphy et al. 2011; Calzetti 2013; Tacchella et al. 2022), or long-term tracers ($\sim$100 Myr) such as far-infrared (FIR) or sub-mm continuum (see reviews by Kennicutt 1998; Kennicutt & Evans 2012). This difference in time-scales between AGN activity and star formation measurements likely contributes to the wide range of findings on the AGN-SFR relationship in the literature. For example, Rosario et al. (2012) found that the connection between FIR luminosity (an SFR indicator) and AGN accretion rate depends on both AGN luminosity and redshift. At high redshifts, in particular, there appears to be no clear relationship between FIR-based SFR and AGN accretion activity. However, spatially resolved studies of Hα emission in a few galaxies suggest that AGN outflows may either suppress or enhance star formation locally, on sub-kiloparsec to kiloparsec scales (e.g. Cano-Díaz et al. 2012; Cresci et al. 2015; Carniani et al. 2016; Bessiere & Ramos Almeida 2022; Kakkad et al. 2023b), a result also supported by recent zoom-in simulations (see Mercedes-Feliz et al. 2024).

Molecular gas, however, offers a promising alternate avenue for assessing the impact of AGN feedback in galaxies. Since stars form from cold molecular gas, AGN-driven outflows, whether by radiation pressure or jets, are likely to impact the molecular gas first. These outflows could sweep up and eject the cold gas ('ejective' feedback), or increase the temperature or turbulence within the gas ('preventative' feedback). Recent simulations with EAGLE suggest that AGN host galaxies contain larger molecular gas reservoirs compared to star-forming galaxies. For example, Ward et al. (2022) investigated the molecular gas content of quasars in three cosmological simulations, namely EAGLE (Schaye et al. 2015), IllustrisTNG (Nelson et al. 2019), and SIMBA (Davé et al. 2019) and concluded that AGN host galaxies should have similar or enhanced molecular gas fractions compared to mass-matched inactive galaxies (or normal star-forming galaxies), both at $z = 0$ and $z = 2$. However, observations present conflicting results. Atacama Pathfinder Experiment telecope (APEX)-based CO observations of low-redshift, X-ray-selected AGN host galaxies (e.g. Koss et al. 2021) support the idea that AGN often reside in gas-rich environments. In contrast, other studies report no significant difference in local molecular gas content between AGN hosts and mass-matched star-forming galaxies at low redshift (e.g. Husemann et al. 2017; Rosario et al. 2018), or even suggest that AGN host galaxies have lower molecular gas content in their central regions compared to the rest of the galaxy (e.g. Ellison et al. 2021; García-Burillo et al. 2024). At Cosmic Noon, follow-up campaigns using Atacama Large Millimeter/submillimeter Array (ALMA) and Northern Extended Millimeter Array (NOEMA) have indicated faster gas depletion in AGN hosts compared to star-forming galaxies (e.g. Kakkad et al. 2017; Bischetti et al. 2021; Circosta et al. 2021; Bertola et al. 2024; Frias Castillo et al. 2024).

The studies mentioned above predominantly use different excitations of the CO molecule as tracers for cold molecular gas (see reviews by Carilli & Walter 2013; Saintonge & Catinella 2022). This cold phase of molecular gas is at temperatures of $T \leq 100$ K. But in turbulent environments with strong AGN radiation, gas can be excited to higher temperatures, a phenomenon extensively studied in the context of galaxy clusters (see McNamara & Nulsen 2007; Fabian 2012). This is especially relevant at Cosmic Noon, where heightened accretion and star-forming activity may result in a larger fraction of molecular gas excited to warm ($T \sim 500$ K) or hot ($T \sim 1000 - 3000$ K) phases. The warm molecular gas is typically traced via rotational transitions of the H_2 molecule in rest-frame mid-infrared spectra (e.g. Armus et al. 2023; Hernandez et al. 2023; Esparza-Arredondo et al. 2025). In this paper, we focus on the hot molecular gas phase at traced by the ro-vibrational transitions of H_2 in rest-frame near-infrared spectra, particularly the 1–0 S(1) and 1–0 S(0) transitions at 2.12 and 2.22 μm, respectively (e.g. Black & van Dishoeck 1987; Elmegreen 1989; Hollenbach & McKee 1989; Maloney, Hollenbach & Tielens 1996; Rosario et al. 2019; Riffel et al. 2021, 2023).

At low-redshift, these ro-vibrational and rotational transitions have been extensively observed in a variety of galaxies, including galaxies that host AGN-driven outflows (e.g. Davies et al. 2009; Storchi-Bergmann et al. 2009; Friedrich et al. 2010; Dasyra & Combes 2011; Rupke & Veilleux 2013; Ramos Almeida & Ricci 2017; Rosario et al. 2019; Riffel et al. 2021; Armus et al. 2023; Hernandez et al. 2023; Esparza-Arredondo et al. 2025; Ulivi et al. 2025). The picture arising from these low-redshift studies is that near-infrared and mid-infrared H_2 lines are strongly enhanced in cool gas shocked by AGN-driven outflows. Therefore, at high redshift, especially at cosmic noon, where several AGN and star-forming galaxies have been shown to host outflows, the warm and hot molecular gas are expected to be prevalent. Up until the launch of *JWST*, it was not possible to trace such warm and hot molecular transitions at cosmic noon. However, with the unique spectroscopic capabilities of the Medium Resolution Spectrometer (MRS) of the Mid-infrared Instrument (MIRI) onboard *JWST*, it is now possible to trace the rest-frame near-infrared transitions out to cosmic noon and beyond.

In this paper, we present the first-ever detection of the hot molecular gas transition in an AGN host galaxy at $z \sim 2.2$, traced via rest-frame near-infrared ro-vibrational H_2 transitions. The selected target is a hard X-ray AGN source, which hosts kpc-scale ionized gas outflows, traced using the [O III]line and is detected in CO(3-2) transition via ALMA and Atacama Compact Array (ACA) observations. The paper is arranged as follows: Section 2 summarizes the basic properties of the target, followed by a description of *JWST*/MRS mid-infrared spectroscopic and *JWST*/NIRCam near-infrared imaging observations and data reduction in Section 3. The analysis of the mid-infrared spectra and NIRCam images and the corresponding results are presented in Section 4. This is followed by a discussion and concluding remarks in Sections 5 and 6, respectively.

The following cosmological parameters are adopted throughout this paper: $H_0 = 70\,\mathrm{km\,s^{-1}}$, $\Omega_M = 0.3$ and $\Omega_\Lambda = 0.7$. Unless specified, North is up and East is to left in the maps presented.

2 TARGET DESCRIPTION

The target, cid_346 (RA (J2000) = 09:59:43.4, DEC (J2000) = +02:07:07.4, $z = 2.219$: redshift based on CO(3-2)), is part of the SINFONI Survey for Unveiling the Physics and Effect of Radiative feedback (e.g. Circosta et al. 2018; Mainieri et al. 2021) and is located within the COSMOS field (e.g. Scoville et al. 2007; Civano et al. 2016). Publicly available multiwavelength photometric and spectroscopic data have enabled precise determination of the AGN and host galaxy properties through Spectral Energy Distribution (SED) modelling (see Circosta et al. 2018). In this section, we outline the key characteristics of this target, also summarized in Fig. 1, and

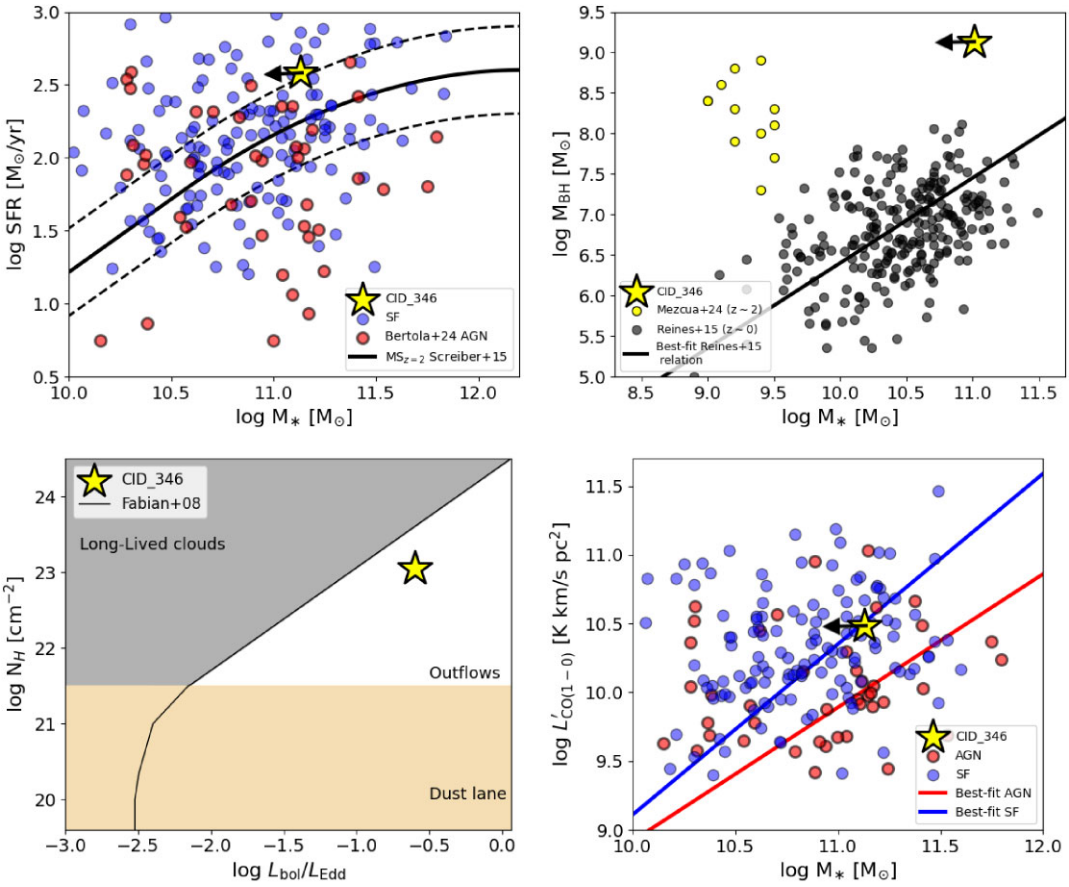

Figure 1. *Top left panel* shows the location of cid_346, at the top end of the star forming main sequence (at $z \sim 2$). The solid line shows the main sequence relation from Schreiber et al. (2015) with 0.3 dex error margins shown as dashed lines. The red and blue data points show the $z \sim 2$ AGN and star-forming galaxies, respectively (e.g. Tacconi et al. 2018; Boogaard et al. 2020; Birkin et al. 2021; Bertola et al. 2024). The *top right panel* shows the location of cid_346 in the $M_{BH} - M_*$ plane. cid_346 is clearly above the $M_{BH} - M_*$ relation for local galaxies (solid black line and black circles from Reines & Volonteri 2015), similar to recent results from cosmic noon (yellow circles from Mezcua et al. 2024) and galaxies at the Epoch of Re-ionization. The *bottom left panel* shows the location of cid_346 in the outflowing region of the N_H versus λ_{Edd} parameter space (see Fabian, Vasudevan & Gandhi 2008). The *bottom right panel* shows cid_346 in the $L'_{CO(1-0)}$ versus M_* plane, with the best-fit lines from Bertola et al. (2024). The colour scheme in the bottom right panel is the same as in the top left panel. For further details, please refer to Section 2.

refer to Circosta et al. (2018, 2021), Vietri et al. (2020), and Bertola et al. (2024)[1] for further details.

cid_346 is classified as a Type-1 AGN, as indicated by the presence of broad lines in its rest-frame ultraviolet (UV) and optical spectra. The black hole mass, estimated from the broad H β line, is log M_{BH} = 9.15 ± 0.30 $M_\odot$ (see Vietri et al. 2020). Stellar mass and SFR, derived through SED modelling, are log M_* < 11.13 $M_\odot$ and 382 ± 37 $M_\odot$ yr^{-1}, respectively (see Bertola et al. 2024). These values position cid_346 at the upper boundary of the star-forming main sequence in the SFR-M_* plane (Fig. 1, top left panel). Its black hole mass is significantly higher than expected based on the local M_{BH}–M_* relation, suggesting that the supermassive black hole in cid_346 may be overmassive relative to its host galaxy (Fig. 1, top right panel). This phenomenon, where overmassive black holes are observed, has been reported in recent studies in galaxies at the Cosmic Noon to the Epoch of Re-ionization (e.g. Übler et al. 2023; Mezcua et al. 2024). The position of cid_346 in these scaling relations, in conjunction with mid-infrared data and comparisons to other AGN host galaxies, will be discussed in a forthcoming paper.

The bolometric luminosity of the AGN in cid_346 is log L_{bol} = 46.66 ± 0.02 erg s^{-1}. Based on the black hole mass reported earlier, the Eddington ratio of the AGN, λ_{Edd} (where $\lambda_{Edd} = L_{bol}/L_{Edd}$ and $L_{Edd} = 1.3 \times 10^{38} \times M_{BH}/M_\odot$ erg s^{-1}), is 0.25. Additionally, X-ray spectral analysis reveals that cid_346 hosts a highly obscured AGN, with an X-ray column density log $N_H = 23.05^{+0.17}_{-0.19}$ cm^{-2}. We place these values in the N_H versus λ_{Edd} plane, within the context of empirical models of outflows in dusty ISM from Fabian et al. (2008) in Fig. 1. Below log N_H = 21.5 cm^{-2} (horizontal line in lower left panel in Fig. 1), dust lanes from the host galaxy could contaminate the column density values. The empirical continuous line in the figure divides the region where Eddington ratio experienced by the cloud is below the Eddington limit (grey shaded region) or above the Eddington limit (unshaded region), the latter defined as the 'forbidden region' for long-lived clouds or 'blowout region' (see also Kakkad et al. 2016; Ricci et al. 2017). cid_346 falls within the unshaded region of the N_H versus λ_{Edd} plot, and is therefore expected to experience an outflow.

cid_346 has been the focus of several observational campaigns using various ground-based telescopes to trace extended ionized and cold molecular gas. A brief overview of these observations is

[1]The SED fitting results for cid_346 were updated in Bertola et al. (2024) using the latest releases of the photometric catalogues for the COSMOS field (Jin et al. 2018; Weaver et al. 2022).

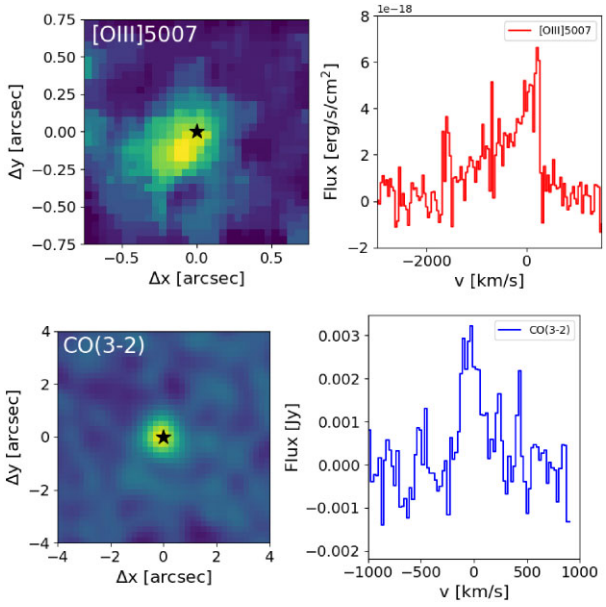

Figure 2. The *top panels* show the [O III]flux map (left) and the integrated spectrum covering the entire region of the [O III] emission (right). The [O III] is extended towards the SE of the AGN location (marked by black star) and its spectrum shows a prominent blue-wing, indicative of ionized outflows. The *bottom panels* show the ALMA CO(3-2) flux map (left) and the corresponding integrated spectrum (right). Further details about the ionized and molecular gas properties are described in Section 2.

provided below, with key results relevant to this paper summarized in Fig. 2.

(i) Observations with Spectrograph for INtegral Field in the Near Infrared (SINFONI) aboard the Very Large Telescope (VLT) provided near-infrared spatially resolved IFS of cid_346 in the *H*-band, which revealed ionized gas outflow traced by [O III], extending up to ∼4 kpc in the southeast direction from the nucleus. This extended outflow is further confirmed through Point Spread Function (PSF)-subtraction techniques (e.g. Kakkad et al. 2020). The outflow velocity exceeds 1000 km s^{-1}, indicating that the AGN is driving the outflow. Based on the outflow model described in Kakkad et al. (2020), the ionized gas mass outflow rate, $\dot{M}_{\rm out}$, is estimated to be between 0.6–15 $M_\odot$ yr^{-1}. This is significantly lower than the star formation rate of ∼380 $M_\odot$ yr^{-1}, suggesting that there is still sufficient gas in the host galaxy to support ongoing star formation despite the fast outflow.
SINFONI *K*-band IFS observations revealed that Hα emission is associated with the Narrow Line Region (NLR) outflow, as it extends in the same direction as the ionized gas, with FWHM (full width at half-maximum) >600 km s^{-1}. A resolved BPT (Baldwin, Phillips, & Terlevich: Baldwin, Phillips & Terlevich1981) map of the extended gas, combined with the [O III]results from the *H*-band, indicates that this emission is most likely ionized by the AGN, based on emission line ratio diagnostic diagrams commonly used for the local universe (e.g. Kewley et al. 2001; Kauffmann et al. 2003).

(ii) cid_346 was also observed with low-spatial resolution (∼1.1 arcsec) ALMA Band-3 to observe CO(3-2) transition to trace the total cold molecular gas content (see Circosta et al. 2021). The CO(3-2) luminosity of cid_346, log $L'_{\rm CO(3-2)}$, was estimated to be 10.25 K km s^{-1} pc^2. Assuming an excitation correction ($r_{31} = L'_{\rm CO(3-2)}/L'_{\rm CO(1-0)}$) of 0.59 and a CO to molecular gas conversion factor, $\alpha_{\rm CO}$, of 3.6 $M_\odot$/(K km s^{-1} pc^2), the total cold molecular gas content in cid_346 is log $M_{\rm mol} = 11.10 \pm 0.05\,M_\odot$. The CO-based cold gas to M_* ratio is consistent with the loci of star-forming galaxies in the $L'_{\rm CO(1-0)}$ versus M_* plot shown in the bottom right panel of Fig. 1. The background blue and red points are obtained from a compilation of molecular gas studies in star-forming and AGN host galaxies in Bertola et al. (2024) (see also Tacconi et al. 2018; Boogaard et al. 2020; Birkin et al. 2021), which uses the following excitation corrections: $r_{41} = 0.37$, $r_{31} = 0.59$, $r_{21} = 0.68$ (e.g. Kirkpatrick et al. 2019). This plot confirms that cid_346 contains an abundance of molecular gas for sustained star formation or for feeding the central supermassive black hole.

(iii) Follow-up ACA observations of cid_346 were obtained in order to map the large scale CO emission out to the circum-Galactic Scales (CGM, >100 kpc, see Cicone et al. 2021). Although the extension of CO gas out to CGM scales was later disputed in Jones et al. (2023), these observations reveal that cid_346 hosts extended molecular gas out to at least tens of kiloparsec scales. At the time of publishing these results, no evidence of merging companions were detected close to cid_346. Therefore, one of the possible explanations put forward was that the outflows from the AGN might relocate the molecular gas out to CGM scales.

Fig. 2 presents a summary of the [O III]λ5007 and CO(3-2) images and spectra from SINFONI and ALMA observations, respectively. The observations summarized above came from ground-based observatories, which were limited in spatial resolution and depth. However, they consistently pointed to the presence of extended gas in the ionized and molecular phases. The ionized gas phase is believed to be part of the extended NLR of cid_346. However, with the launch of *JWST*, it has become possible to trace rest-frame optical and near-infrared emissions with unprecedented spatial resolution and depth, surpassing even the best Adaptive Optics capabilities of ground-based telescopes.

3 OBSERVATIONS AND DATA REDUCTION

3.1 *JWST* MIRI/MRS observations and data reduction

cid_346 was observed with MIRI/MRS aboard *JWST* as a part of Cycle-1 GO programme 2177 (PI: Mainieri). Target acquisition was not required during the observations as the pointing accuracy of 0.1 arcsec is sufficient to locate the target in the MRS field-of-view. Furthermore, we employed a 4-point dither pattern, which enhanced the spatial sampling and spatial resolution in the final drizzled data cube (see Law et al. 2023). We also took dedicated background exposures for background subtraction, as the contribution of infrared background is substantial in Channels 3 and 4.

The MRS observations were carried out on 2023 November 20 in the LONG band. The LONG band simultaneously covers the wavelength ranges 6.53–7.65, 10.02–11.70, 15.41–17.98, and 24.19–27.90 μm in Channels 1, 2, 3, and 4 respectively. At the redshift of cid_346, these correspond to rest-frame wavelength ranges of 2.02–2.37, 3.11–3.63, 4.78–5.58, and 7.51–8.66 μm in the respective channels. The respective resolving power, *R*, in each channel is 3100–3610, 2860–3300, 1980–2790, and 1630–1330. The observations employed a SLOW readout mode in 38 groups per integration, 3 integrations per exposure, and 12 exposures. As a result, the final total exposure time on-source was 11 084 s (∼3.07 h).

We mostly follow the standard MRS data reduction procedure, as set by the pipeline (e.g. Labiano et al. 2016) with additional customized steps and fine-tuning parameters to improve data quality. We reduced the data using the *JWST* pipeline version 1.17.1. The

data reduction steps are briefly summarized here. The pipeline runs in three stages. The first stage of the MRS pipeline performs the detector-level corrections. We kept most of the default pipeline parameters unchanged, except we set the `find_showers` keyword to `TRUE`. This step identifies and corrects the Cosmic Ray showers. To improve the identification of warm pixels, which may have been missed in the stage-1 data reduction, we derived the median of all slope images of each detector and applied a classical sigma clipping algorithm. The newly identified bad and warm pixels were masked in the bad pixel mask as `DO_NOT_USE`. The output of the first stage is a set of corrected count rate files, which are then processed with the second stage of the pipeline. The second stage performs instrument calibrations such as wavelength calibration, flat-field correction, flux calibration and removes fringes. For the second stage, the default pipeline parameters were unchanged, except the `skip_residual_fringe` parameter, which was set to `FALSE` (Default is `TRUE`). This parameter corrects the fringing patterns in the individual channels. The background subtraction was performed using dedicated background exposures. The second stage of the MRS pipeline outputs a set of fully calibrated individual exposures. These fully calibrated exposures are then finally fed into the third stage of the pipeline, where these calibrated exposures across different wavelength bands and channels are combined into a final drizzled data cube. The parameters for the third stage were also kept unchanged, except the `skip_outlier_detection` was set to `FALSE`, with the outlier threshold kept at 99 per cent, which removes any significant remaining outliers in the data when combining different exposures.

The final products from the three stages of the pipeline consist of a set of four data cubes, corresponding to the four channels of the LONG configuration. The field-of-view in channels 1, 2, 3, and 4 are $\approx 3.2 \times 3.7$, 4.0×4.8, 5.2×6.2, and 6.6×7.7 arcsec^2, respectively. The corresponding spatial resolution of the channels are $\approx$0.18, 0.28, 0.39, and 0.64 arcsec, respectively.

3.2 NIRCam and ACS imaging from COSMOS

cid_346 was also observed as a part of the COSMOS-Web survey, a *JWST* Cycle-1 treasury programme (GO-1727, PI: Kartaltepe & Casey, see Casey et al. 2023 for an overview). The COSMOS-Web survey covered 0.54 deg^2 of the COSMOS survey (e.g. Scoville et al. 2007) with four filters of the NIRCam instrument (F115W, F150W, F277W, F444W; Rieke et al. 2023). In this paper, we use the NIRCam imaging of cid_346 to compare with the H_2 maps in the MRS data in Section 4.

The NIRCam observations were taken in April 2023, and the data were processed using the *JWST* Calibration Pipeline version 1.14.0[2] (see Bushouse et al. 2024) and the Calibration Reference Data System version 1223. In addition to NIRCam imaging, we also used the publicly available archival HST/ACS (Advanced Camera for Surveys) F814W imaging (Koekemoer et al. 2007). The NIRCam and ACS images have a pixel scale of 0.03 arcsec pixel^{-1}.

4 ANALYSIS AND RESULTS

In this section, we present the detection of the hot molecular gas via ro-vibrational transitions in the MRS spectra. Furthermore, we will present evidence for the presence of companions close to cid_346, with the help of ancillary NIRCam imaging data from COSMOS-Web. Finally, we will compare the MRS and NIRCam results with ground-based SINFONI and ALMA observations of this target.

[2]https://github.com/spacetelescope/jwst

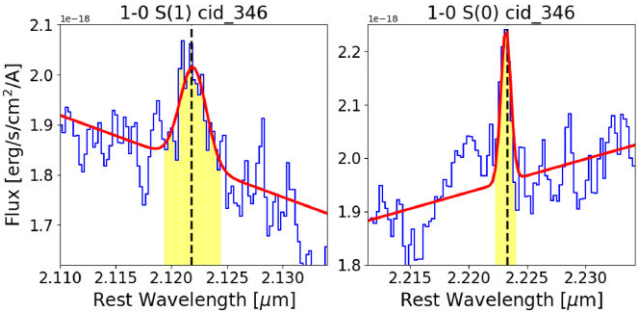

Figure 3. 1-0 S(1) and 1–0 S(0) detections in the central AGN, cid_346. The blue curve shows the data extracted from the MRS cubes, the red curve shows the single Gaussian models to the emission lines, along with local continuum, and the yellow shaded region shows the spectral window containing ∼95 per cent ($\pm 2\sigma$) of the emission line flux. The black dashed line shows the expected location of each line, based on the redshift of cid_346.

4.1 Detection of hot molecular gas

Before the launch of *JWST*, sensitive mid-infrared spectrographs were unavailable, making MRS spectroscopy a unique opportunity to study the rest-frame near-infrared spectra of galaxies, particularly at Cosmic Noon. Among the various lines within near-infrared and mid-infrared wavelengths, the ro-vibrational and rotational transitions of hydrogen molecules are used as tracers of molecular gas at temperatures from a few hundred to several thousand Kelvin. In this paper, we focus on the hot H_2 phase in the rest-frame near-infrared wavelengths, that could be excited by fluorescence soft-UV photons in both star forming and AGN-ionized regions (e.g. Black & van Dishoeck 1987) or via thermal processes from X-ray or shock heating (e.g. Hollenbach & McKee 1989; Maloney et al. 1996).

We are particularly interested in the 1–0 S(1) transition at rest-wavelength 2.12 μm (we use the notation 1–0 S(1) and H_2 2.12 μm interchangeably), commonly used to trace hot molecular gas in nearby galaxies and falls in channel-1 LONG sub-band. Therefore, we first extract the channel-1 LONG spectra from the AGN location, identified using the peak of the continuum emission, using a circular aperture of radius ∼0.4 arcsec. This aperture size approximately covers the spatial extent of the central host galaxy (we detect extended gas components, which are discussed later). In order to trace possible residual instrument response feature in the MRS spectra, we also selected three object-free regions, randomly selected in the data cube, from where spectra were extracted and compared with the target spectrum. This procedure was also used to confirm the line detections described here. A comparison between the target spectrum and spectrum from one of the object-free locations is shown in Fig. A1.

Following this comparison, we confirm detections of the 1–0 S(1) and 1–0 S(0) transitions in cid_346 at $\sim 4\sigma$ levels each. A zoom-in of the extracted MRS spectra around these transitions is shown in Fig. 3 in blue. We model these H_2 lines using a single Gaussian function, along with a linear continuum that models the local continuum within the spectral window centred on the individual transitions. We do not impose any constraints while fitting these Gaussian profiles to the emission lines, with the exception that the line peak intensities are positive. The Gaussian models to the emission lines are shown

Table 1. Detected H_2 ro-vibrational transitions tracing the hot molecular gas in the central AGN host, cid_346 and locations C1 and C2 (see Fig. 5). (a) Reports the ro-vibrational H_2 transition, (b) reports the expected rest-frame wavelength of the transition, based on the redshift quoted in Circosta et al. (2021), (c) reports the actual wavelength of the transition, based on the centroid location of the Gaussian fit to the line, (d) shows the shift of the measured line location with respect to the expected location. + means the line is red-shifted and − means the line is blue-shifted, (e) reports the line width (FWHM), (f) shows the line flux and (g) reports the signal-to-noise (SNR) of the detected line. Parameters reported in columns (c), (d), and (e) are from single Gaussian fits, as described in Section 4.1. The errors represent 1σ deviation from the quoted values.

Transition	Expected wavelength (μm)	Actual wavelength (μm)	Red/Blue-shift (+ /−)(km s^{-1})	FWHM (km s^{-1})	Flux (10^{-18} erg s^{-1} cm^{-2})	SNR
(a)	(b)	(c)	(d)	(e)	(f)	(g)
cid_346						
1–0 S(1)	2.1218	2.1220 ± 0.0002	23 ± 22	458 ± 60	5.7 ± 0.8	4.1
1–0 S(0)	2.2233	2.2232 ± 0.0001	-8 ± 8	130 ± 20	2.6 ± 0.4	4.4
C1						
1–0 S(1)	2.1218	2.1209 ± 0.0003	-130 ± 40	500 ± 125	2.5 ± 0.6	2.4
C2						
1–0 S(1)	2.1218	2.1223 ± 0.0004	67 ± 24	127 ± 61	1.6 ± 0.5	4.1

in red in Fig. 3 and the yellow regions mark the flux containing 95 per cent of the emission line flux ($\pm 2\sigma$). To estimate the errors in our measurements, we generated 100 mock spectra by adding Gaussian random noise to the modelled spectra, using the standard deviation of line-free regions of the spectra. The fitting procedure described earlier was then applied to each of these mock cubes without imposing any parameter constraints. The associated error is given by the standard deviation of these 100 measurements. The parameters corresponding to the Gaussian models, namely the line centroid, width (FWHM) and the fluxes are reported in Table 1.

At the sensitivity of the MIRI/MRS data, we do not detect the presence of extended wings in the spectral profiles of the H_2 transitions. This is confirmed by the fact that it was not necessary to add a second Gaussian component during the line fitting. The width (FWHM) of the 1–0 S(1) and 1–0 S(0) are 458 ± 60 and 130 ± 20 km s^{-1}, respectively. Given a resolving power of $\sim$100 km s^{-1} at the location of these lines, the transitions are well resolved. In previous studies, a cut of 600 km s^{-1} has usually been employed to distinguish between gas outflows in the ionized phase that are driven by an AGN or not (e.g. Kakkad et al. 2020; Wylezalek et al. 2020; Tozzi et al. 2024). This value is based on the maximum velocity dispersion one expects in a purely rotating disc in a star-forming galaxy. The transitions reported in the MRS spectra do not cross this threshold. It is also possible that the observations did not have sufficient depth to detect the presence of faint wings beneath the emission line profiles. However, we note that the bulk of the molecular gas, whether based on CO or ro-vibrational transition, may be dominated by gas in the host galaxy disc (see also Barfety et al. 2025). In addition, simulations by Ward et al. (2024) showed that in the presence of a clumpy ISM, the outflow can cover a broad range of velocities, with a considerable fraction of mass moving below 100 km s^{-1}. Therefore, the cut of 600 km s^{-1} used in case of the ionized gas, largely coming from the NLR, may not be applicable here. The H_2 line widths reported in Table 1 are significantly narrower than that of [O III]-based ionized gas from ground-based IFS observations, which show a FWHM of $>$1500 km s^{-1}.

We find the flux ratio, 1–0 S(1) to 1–0 S(0), to be $\sim 2.2 \pm 0.7$. The S(1):S(0) flux ratio can be used to determine the temperature of the hot molecular gas and a comparison between samples spanning a wide range of redshift and luminosity can provide clues into the impact of the presence of AGN on the molecular gas temperatures, discussed later in this section. We compare the 1–0 S(1) to 1–0 S(0) flux ratio in cid_346 with measurements in low-redshift AGN host galaxies from Riffel, Rodríguez-Ardila & Pastoriza (2006) and

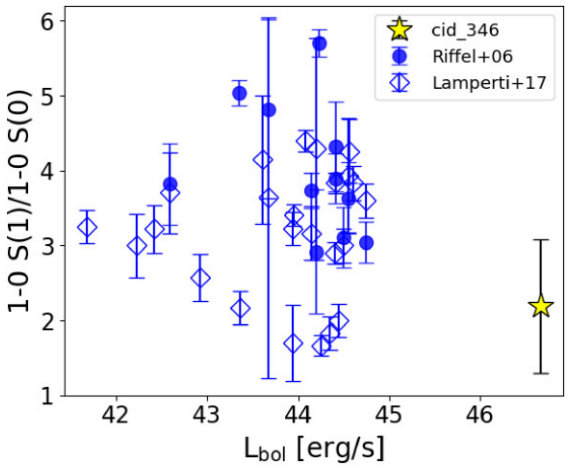

Figure 4. 1-0 S(1) to 1–0 S(0) line ratio in cid_346 (yellow star) and low-redshift Seyfert galaxies (blue circles) as a function of the bolometric luminosity. The error bars represent 1σ uncertainties in the respective line ratios.

Lamperti et al. (2017) in Fig. 4. Riffel et al. (2006) consists of a compilation of near-infrared spectra of 47 $z < 0.5$ AGN and Lamperti et al. (2017) consists of a compilation of 102 $z < 0.075$ X-ray selected AGN from BAT (Burst Alert Telescope) AGN Spectroscopic Survey (e.g. Koss et al. 2017). Fig. 4 shows only those low-redshift targets from these studies which have detections and/or upper limits on both 1–0 S(1) and 1–0 S(0) transitions. Both studies consist of measurements from type-1 and type-2 AGN. Our measured flux ratio for cid_346 is within the range of typical flux ratios of the two lines observed in the comparison low-redshift AGN host galaxies. The line ratio also appears to be at the lower end of the range seen in low-redshift galaxies. However, this is based on a single galaxy at the high luminosity end and that we need more number statistics at these higher luminosities, especially for $L_{bol} > 10^{45}$ erg s^{-1}, to confirm the trend. Further details on the possible origin of the H_2 emission in cid_346 are discussed in Section 5.

We can use the 1–0 S(1) and 1–0 S(0) transitions to constrain the hot gas temperature using the following equation (e.g. see Wilman, Edge & Johnstone 2005):

$$\log\left(\frac{F_i \lambda_i}{A_i g_i}\right) = \text{constant} - \frac{T_i}{T_{exc}} \quad (1)$$

In eq. (1), F_i represents the flux of the ith H_2 transition, λ_i is the associated wavelength, A_i denotes the spontaneous emission coefficient, g_i is the statistical weight of the upper level of the transition, T_i refers to the energy of the level expressed as a temperature, and T_{exc} is the kinetic temperature assuming the H_2 is in equilibrium. Using the equation above for the 1–0 S(1) and 1–0 S(0) transitions, we derive a hot gas temperature of 1100^{+465}_{-245} K for the central source cid_346.

We can also estimate the mass of the hot molecular gas using 1–0 S(1) transition at 2.12 μm, adopting the standard prescriptions used for low-redshift galaxies in the literature (Storchi-Bergmann et al. 2009; Riffel et al. 2023). The choice of 1–0 S(1) transition is motivated by the fact that it is one of the strongest ro-vibrational transitions. As a result, there are several low-redshift observations of this line for which the calculation is well-established and would make it ideal for comparing our mass measurements. Specifically, we use the following equation to determine the mass of the hot H_2 gas:

$$M_{H_2} = \frac{2\, m_p F_{2.12}\, 4\pi D_L^2}{f_{v=1,J=3} A_{S(1)} h\nu} \quad (2)$$

where m_p is the proton mass, $F_{2.12}$ is the flux of the 1–0 S(1) line, D_L is the luminosity distance, f is the population fraction and $A_{S(1)}$ is the transition probability. The population fraction is obtained directly from quantum mechanical principles and we obtain transition probabilities from Turner, Kirby-Docken & Dalgarno (1977) (see also Wolniewicz, Simbotin & Dalgarno 1998 and Roueff et al. 2019). For the vibrational temperature of $T \sim 1100^{+465}_{-245}$ K, $f_{v=1,J=3}$ takes values between $1 - 7.5 \times 10^{-3}$. Using the flux of the 1–0 S(1) line reported in Table 1 into eq. (2), we obtain a hot H_2 gas mass of $5.0^{+7.0}_{-3.5} \times 10^5\, M_\odot$ in cid_346.

We can now compare the mass of the molecular gas in cold phase (<100 K) to the hot phase (∼1000—3000 K). The total amount of CO-based cold gas in the cid_346 system is $1.2 \times 10^{11} M_\odot$ (see Circosta et al. 2021). The ratio between the CO-based cold molecular gas mass and the H_2 2.12 μm-based hot molecular gas mass is $\approx 10^5 - 10^6$, i.e. the CO-based cold gas mass is nearly six orders of magnitude larger than the H_2 2.12 μm-based hot gas mass, similar to the values seen in some of the low-redshift galaxies (e.g. Pereira-Santaella et al. 2016; Emonts et al. 2017). We further discuss the comparison of cold-to-hot gas mass ratios with low redshift galaxies in Section 5.

4.2 Extended hot molecular gas

In this section, we present channel maps of the brighter 1–0 S(1) line and search for the presence of extended hot molecular gas emission. Fig. 5 shows the hot molecular gas map, obtained by collapsing the channels containing 1–0 S(1) emission. The hot molecular gas appears extended beyond the MRS PSF and the observed spatial extent is observed in approximately the same direction as the [O III]-based ionised gas reported in Kakkad et al. (2020). In particular, we identified two locations, which we name C1 and C2 approximately 1.0 (∼8.2 kpc) and 2.0 (∼16.4 kpc) arcsec from the AGN location, respectively, (also marked in Fig. 5), where the hot molecular gas emission is prominent. Within the current scope of this paper, we do not attempt to decompose emission contributions from the QSO and host galaxy separately (e.g. Chen et al. 2024) and will be implemented in future studies utilising this MIRI-MRS data. This would also facilitate a direct comparison with existing ground-based ancillary near-infrared IFS and sub-mm data.

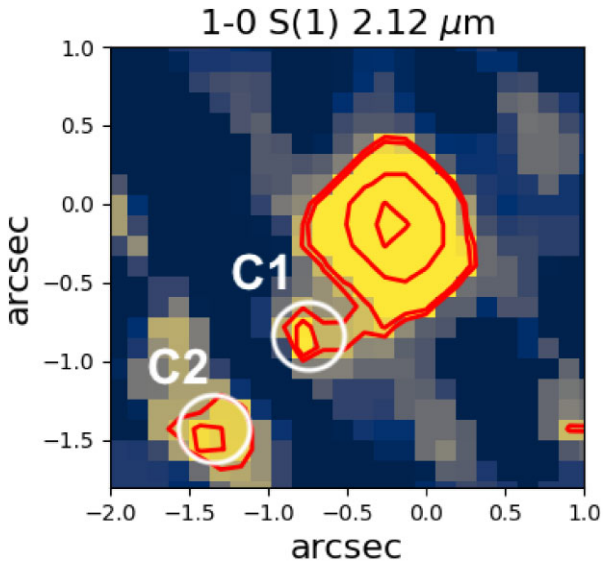

Figure 5. 1-0 S(1) channel map obtained by collapsing the channels centred on 2.12 μm emission. The red contours show emission above 3σ. The H_2 maps indicate extended clumps of hot gas around cid_346. In addition to the central host, reference spectra were extracted from the locations marked C1 and C2, where the extended emission is detected in most transitions, ∼0.8 and ∼1.5 arcsec away from cid_346, respectively.

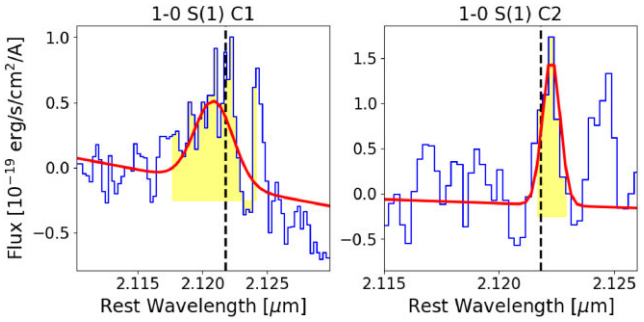

Figure 6. 1-0 S(1) detections in extended regions: the left panel shows spectrum from C1 and the right panel shows spectrum from C2 (see Fig. 5).

We extract MRS spectra from C1 and C2 using circular apertures centred on the respective locations, with a radius of 0.25 arcsec, approximately corresponding to the PSF of the MRS at these wavelengths.[3] The size of the apertures were manually chosen to roughly correspond to the extent of the emission in each spatial component. We detect 1–0 S(1) emission in C1 and C2 at 2.4σ and $\sim 4\sigma$, respectively (see Figs 5 and 6 and Table 1). The 1–0 S(0) component remained undetected in the extended regions.

Having detected the extended hot molecular gas in the MIRI/MRS data in the same direction as the extended ionized gas in VLT/SINFONI data, we re-analysed the archival ALMA CO(3–2) data of cid_346 (Project code: 2016.1.00798.S) to search for extended cold molecular gas component in the SE direction of the AGN. The details of the ALMA programme from which we obtained the data are available in Circosta et al. (2021). The left panel in Fig. 7 shows the detection of diffuse and extended CO(3–2) emission, located >2.0 arcsec from cid_346 at $\sim 3\sigma$ significance level. We

[3] https://jwst-docs.stsci.edu/jwst-mid-infrared-instrument/miri-operations/miri-dithering/miri-mrs-psf-and-dithering

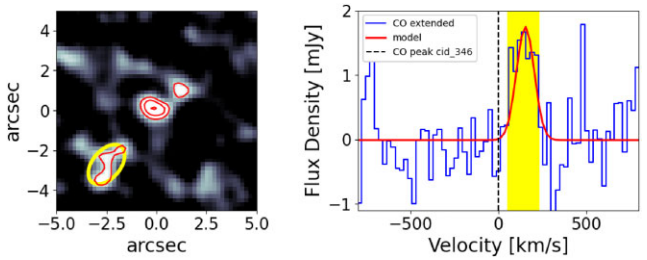

Figure 7. The left panel shows a diffuse extended CO(3-2) emission towards the SE of cid_346 at (0,0) arcsec. The red contours show the CO emission at levels $3\sigma, 4\sigma$, and 5σ. The spectrum extracted from the yellow circle, covering the extended CO emission, is shown in the right panel. The blue curve in the right panel shows the data and the red curve shows the Gaussian model to the emission line. The dashed black line shows the location of the CO(3-2) peak emission from cid_346 (see also Circosta et al. 2021), suggesting that the extended CO(3-2) emission is red-shifted with respect to cid_346.

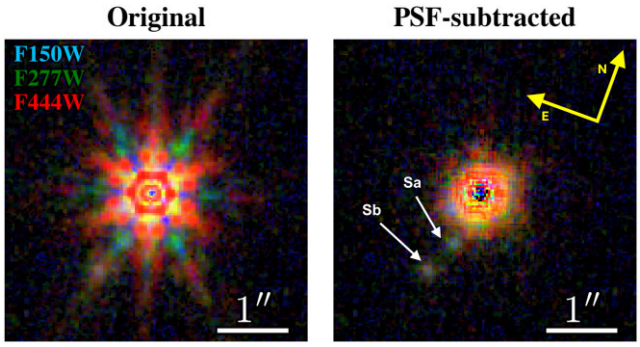

Figure 8. The left panel shows the combined multicolour image from the raw NIRCam image filters F150W, F277W, and F44W and the right panel shows the corresponding PSF-subtracted image where the two companions, Sa and Sb, are clearly visible.

extracted a spectrum from a circular aperture covering the extended CO emission, shown as a yellow circle in Fig. 7. The extracted CO spectrum is shown in the right panel of Fig. 7. The peak location of the extended CO component is red-shifted by $\sim$120 km s^{-1}. The width of the extended CO component is 120 km s^{-1}, compared to a width of 201 km s^{-1} observed in cid_346.

Following the procedure described in Section 4.1, we calculate the gas mass in the extended regions, C1 and C2, to be $1.5^{+2.3}_{-1.1} \times 10^5$ M$_\odot$ and $1.6^{+2.3}_{-1.1} \times 10^5$ M$_\odot$, respectively. Along with the central host, cid_346, the total hot molecular gas in cid_346 system is $\sim 8.4 \times 10^5$ M$_\odot$. Most of the hot molecular gas ($\sim$60 per cent) is concentrated in the central AGN itself, while the rest of the hot gas is in the extended regions. Similarly, the total amount of CO-based cold gas in the cid_346 system is 1.5×10^{11}M$_\odot$, out of which $\sim$80 per cent is from cid_346 (1.2×10^{11} M$_\odot$, see Circosta et al. 2021), while the rest 20 per cent is from the extended component. Even after accounting for these extended components, cold molecular gas dominates the mass budget.

4.3 Companions around cid_346 with NIRCam imaging

As described in Section 3.2, cid_346 was also covered as a part of the COSMOS-Web imaging campaign. Given the extended ionised, hot and cold molecular gas, we explored the imaging data to search for the presence of possible companions around cid_346.

JWST/NIRCam images are contaminated by PSF-diffracted spikes. Therefore, we cannot visually identify the presence of extended component in the host galaxy or possible presence of companions in each of the filters (F150W, F277W, and F444W) of NIRcam raw images (see left panel in Fig. 8). Therefore, we perform PSF-subtraction based on the methods outlined in Tanaka et al. (2024) and briefly mentioned here. NIRCam PSFs were constructed using `PSFEx` (see Bertin 2011) that empirically models PSF based on stars detected from applying SExtractor software package (see Bertin & Arnouts 1996). We fit the images from each NIRCam band with a composite model consisting of a single PSF component and additional Sérsic components. The number of additional components required was decided based on the lowest Bayesian Information Criterion (see Schwarz 1978).

We required a total of three Sérsic components to fit the cid_346 system. The first Sérsic component was required for the host galaxy of the AGN itself. In addition, we fit two other Sérsic components, which we refer as Sa and Sb, corresponding to two companions which are detected towards the SE of the AGN location. We estimate the error of the fitted parameters using χ^2_υ-based weighting of each single PSF, following the approach of Ding et al. (2020). Table 2 reports the values of the parameters n, r_e, flux, and S/N of each of the components estimated from the above four-component fitting.

The left panel of Fig. 8 shows the raw NIRCam multicolour image combining the filters F150W, F277W, and F444W and the right panel shows the PSF-subtracted multicolour image where the two components are detected. Based on the F277W results, the centre positions of Sa and Sb are (RA (J2000) = 09:59:43.4, DEC (J2000) = +02:07:06.5) and (RA (J2000) = 09:59:43.4, DEC (J2000) = +02:07:06.0), respectively, which are offset by $\sim$0.8 arcsec ($\sim$6.6 kpc) and $\sim$1.4 arcsec ($\sim$11.6 kpc) from the host galaxy. The raw images of the individual NIRCam images and the PSF subtracted images are moved to the appendix (see Fig. A2).

The indications of companions (or satellite galaxies), along with extended multiphase gas in cid_346 suggests that this galaxy may be in a minor merger. Although we will later show that the components, C1 and C2, in H_2 emission discussed in Section 4.2 do not directly align with the Sa and Sb detected in NIRCam images (right panel in Fig. 10), the presence of companions may explain the extended gas reservoir seen in cid_346 (see also Cicone et al. 2021). We also estimate the properties of each companion using SED fitting, following the methods in Tanaka et al. (2024). We briefly describe the procedure here. We fit the photometric fluxes of each component using `CIGALE-v2022.1` SED fitting library (see Boquien et al. 2019; Yang et al. 2022). As the extended hot molecular gas is detected in a similar direction as the Sa and Sb components, we assume that Sa and Sb are at the same redshift as cid_346. We model the stellar populations using a single stellar population model (by Bruzual & Charlot 2003), assuming a Chabrier initial mass function (Chabrier 2003) with a stellar mass (M_*) range between 0.1 and 100 M$_\odot$. We assume a delayed-τ model for a star-formation history (see eq. 7 in Tanaka et al. 2024). We model the nebular emission using the `nebular` module and dust attenuation using the `dustatt_modified_starburst` module, the latter assuming a modified Calzetti et al. (2000) law. To limit the models within physical solutions, we set the upper limit of t_{age} to $0.95t_H$, where t_H indicates the cosmic age at each redshift. Stellar metallicity, Z_* and the ionization parameter, U, are fixed at Solar metallicity and $\log U = -2$, respectively.

Fig. 9 compares the best-fitting model SED with the photometry of each of the components. We estimate the spectral slope of the AGN component, α ($F_\lambda \propto \lambda^\alpha$), to be $\sim$ 1.5, which is typical for nearby

Table 2. Morphological and photometric parameters of cid_346 system estimated from the four-component image modelling. See Section 4.3 for further details.

Component	n^a	r_e/arcsec^a	m^b_{F814W}	m^b_{F115W}	m^b_{F150W}	m^b_{F277W}	m^b_{F444W}
AGN PSF	–	–	19.3 ± 0.1	19.2 ± 0.1	19.2 ± 0.1	19.3 ± 0.03	18.7 ± 0.02
AGN host	0.8 ± 0.2	0.25 ± 0.01	23.6 ± 0.6	23.1 ± 0.5	21.7 ± 0.3	21.13 ± 0.07	20.5 ± 0.1
Sa	2.5 ± 0.6	0.15 ± 0.05	26.9 ± 0.4	26.3 ± 0.4	25.3 ± 0.2	25.91 ± 0.07	25.1 ± 0.2
Sb	1.3 ± 0.2	0.10 ± 0.01	<27.8	26.8 ± 0.4	26.0 ± 0.2	25.87 ± 0.06	25.9 ± 0.1

[a] n and r_e are the values measured for the F277W image.
[b] AB magnitude (Oke 1974).

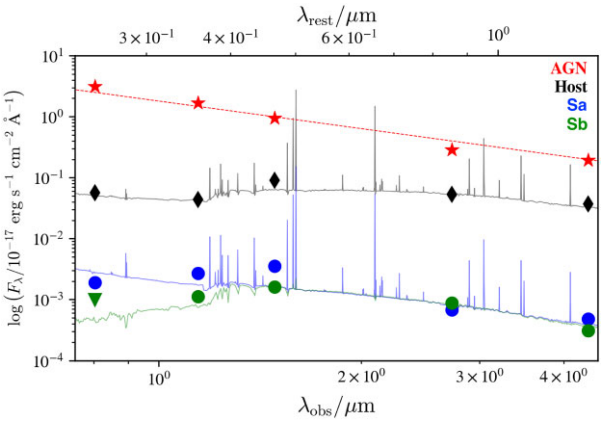

Figure 9. The SED fitting results of cid_346, Sa, and Sb. The red data points and the corresponding curve shows the AGN component of cid_346, the black colours corresponds to the host galaxy of cid_346, the blue colours to Sa and green to Sb.

AGNs (e.g. Vanden Berk et al. 2001). The consistency of the slope with that of nearby AGN validates the decomposition of the AGN and PSF components presented earlier. The components Sa and Sb, on the other hand, exhibit different SED shapes, which may suggest different SFR and dust properties of each of these galaxies. From the SED fitting results, Sa has a SFR $= 1.6 \pm 0.9\,M_\odot\,yr^{-1}$, while Sb has SFR $= 0.5 \pm 0.6\,M_\odot\,yr^{-1}$, suggesting Sa may have higher recent star formation activity than Sb. The stellar mass of the AGN host, log M_*, from the SED fits is $10.9 \pm 0.3\,M_\odot$. This value is consistent with the literature results of cid_346 in Tanaka et al. (2024) and similar to the SED fitting presented in Circosta et al. (2018) and Bertola et al. (2024). The stellar mass of the two companions, Sa and Sb, on the other hand, are log $M_* = 8.9 \pm 0.3\,M_\odot$ and $8.9 \pm 0.2\,M_\odot$, respectively. Although this suggests that the companion galaxies are 100 times less massive than the AGN host itself, the SED fitting presented have large uncertainties and the analysis presented here only indicates the possible presence of a minor merger in cid_346 system. We further discuss the role of possible mergers in driving the AGN activity in Section 5.

5 DISCUSSION

We presented new *JWST* rest-frame near-infrared spectra and NIRCam imaging of cid_346, a luminous AGN at cosmic noon epoch. Fig. 10 shows a summary of the extended emission from the multiwavelength spatially resolved data presented in this paper and in the literature: [O III]-based ionized gas maps from VLT/SINFONI, CO(3–2)-based cold molecular gas maps from ALMA, H_2 2.12 μm-based hot molecular gas from MIRI/MRS and PSF-subtracted NIRCam F277W image. All the gas components i.e. ionized gas, cold and hot molecular gas are extended approximately in the same spatial direction (SE of the AGN). There are differences in the exact locations and extension of the different gas components. VLT/SINFONI observations only probed the inner 1.5 arcsec of the host galaxy (or 0.75 arcsec ≡ 6 kpc from the AGN location). However, based on the cold and hot molecular gas observations, it is possible that the ionised gas might be extended beyond 6 kpc from the AGN. The peak of the extended CO(3–2) emission is seen nearly at the edge of the hot molecular gas clump C2. This suggests a multiphase ionization or gas excitation by the AGN, starting with the warm ionised gas phase (∼10 000–20 000 K), followed by hot molecular (∼1000 K) and cold molecular (<100 K) gas, as one moves away from the AGN location.

Over the last few years, several observations of the cold molecular gas in mass-matched AGN and non-AGN host galaxies at Cosmic Noon have revealed a systematic difference between the CO-based cold molecular gas content in the two classes of galaxies. In these studies, the AGN host galaxies seem to have lower CO-based cold gas mass compared to non-AGN hosts (see Kakkad et al. 2017; Brusa et al. 2018; Circosta et al. 2021; Bertola et al. 2024). A few observations at low-redshift have revealed that molecular gas exists in warm or hot gas phases, where the CO emission is absent (e.g. Rosario et al. 2019; Davies et al. 2024). Our *JWST*/MRS and ALMA observations of cid_346 were mainly motivated to evaluate what fraction of molecular gas may exists in the warm or hot molecular gas phases at cosmic noon, compared to the cold molecular gas phase. The observations presented in this paper may be one of the first detections of H_2 2.12 μm-based hot molecular gas in a galaxy at Cosmic Noon. Here we present some possibilities on the mechanisms in cid_346 that could excite the detected ro-vibrational transitions. The H_2 ro-vibrational transitions in the near-infrared spectra could be excited by non-thermal processes such as fluorescent excitation due to absorption of UV photons (e.g. Black & van Dishoeck 1987) or by thermal processes such as excitation by X-ray heating (e.g. Maloney et al. 1996) or by shocks (e.g. Hollenbach & McKee 1989). Several line ratios and correlations can be used to distinguish between the different excitation mechanisms. For example, the line ratio: H_2 λ2.2477/2.1218 can distinguish between thermal (∼0.1) and fluorescent (∼0.5) excitation mechanisms (e.g. Mouri 1994; Reunanen, Kotilainen & Prieto 2002; Rodríguez-Ardila, Riffel & Pastoriza 2005; Riffel et al. 2008; Storchi-Bergmann et al. 2009). We do not detect H_2 2.2477 μm emission in the MIRI-MRS data of cid_346. However, we calculate an upper limit on the flux ratio H_2 λ2.2477/2.1218 of 0.3, which suggests that the observed H_2 2.12 μm is likely excited by thermal processes. We can also estimate the 2.12 μm flux that can be generated by a given X-ray incident radiation, following Maloney et al. (1996) models. We follow the methodology adopted in Riffel et al. (2008) (see also Zuther et al. 2007; Storchi-Bergmann et al. 2009), calculating the ionisation parameter, ξ_{eff}, using incident hard X-ray flux at distances of ≈100–200 pc from the central source. We calculate the expected emergent H_2 2.12 μm flux in the range $\sim 10^{-18} - 10^{-17}$ erg s^{-1} cm^{-2}, for

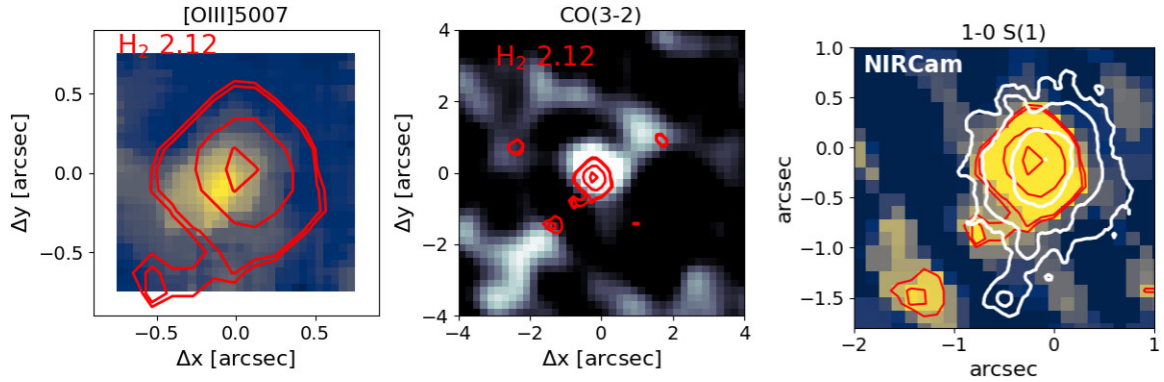

Figure 10. The background image in the *left panel* shows the ground-based [O III]flux map from SINFONI observations (Kakkad et al. 2020), the *middle panel* shows the extended CO(3-2) channel map from ALMA observations from Fig. 7 and the *right panel* shows the 1–0 S(1) map (also shown in Fig. 5). The red contours in the all the panels show the H_2 1–0 S(1) emission at 2.12 μm and the white contours in the right panel show the NIRCam PSF-subtracted contours.

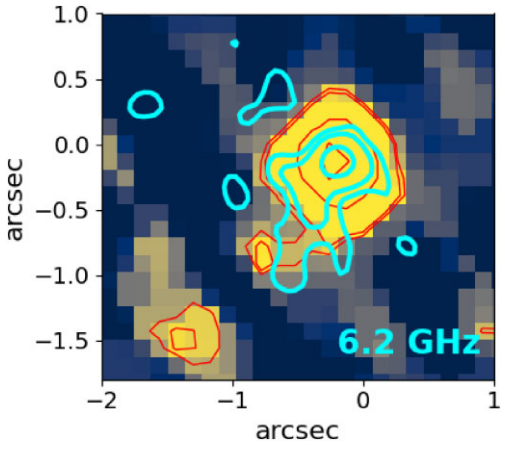

Figure 11. Background image shows the 2.12 μm flux map with 6.2 GHz radio contours from VLA A-array (Ilha et al.).

a ∼0.4 arcsec aperture, the same as the one used to extract the MRS spectrum from the central source in cid_346. Comparing this emergent flux with the observed flux reported in Table 1, it is likely that the X-ray heating from the AGN can account for most of the observed H_2 2.12 μm flux.

Fig. 11 shows the 2.12 μm emission with 6.2 GHz radio contours obtained from Very Large Array (VLA) A-array observations overlaid. We matched the peak of the radio emission and the peak of H2 2.12 um emission for the overlay shown in Fig. 11. The extended radio structure around this source bending approximately at the location of C1 suggests that the C1 component/clump may have been shock-excited due to the radio jet. Even in the central source, the radio jets may contribute to the H_2 emission. Details of the VLA observations will be presented in detail in a forthcoming paper (Ihla et al.). Therefore, in addition to, or alternative to the X-ray radiation from AGN accretion disc, radio jets might deplete CO-based molecular gas while enhancing the emission from hot molecular gas. Coupled with the fact that NIRCam imaging observations suggest cid_346 is in an interacting system, the emerging picture from these observations is that the hot molecular gas forms a part of the larger extended gas reservoir of this merging system of galaxies, that is shock-heated due to the presence of radio jets and is also being ionised by the central AGN.

Using the observed flux and temperature of the H_2 2.12 μm line, we find the total mass of the hot molecular gas phase, calculated using the 2.12 μm emission extracted from cid_346, C1 and C2 (Fig. 5), of $8 \times 10^5\ M_\odot$. The ratio of hot-to-cold molecular gas in cid_346 is $10^{-6} - 10^{-5}$. Using a combination of VLT/SINFONI H_2 2.12 μm and ALMA CO-based observations, Emonts et al. (2017) and Pereira-Santaella et al. (2016) reported a hot-to-cold molecular gas mass ratio of $\sim 6 - 7 \times 10^{-5}$ in low-redshift ($z \sim 0.01$) Luminous Infrared Galaxies (LIRGs) hosting either an AGN or starburst. Although the statistics are low, comparing our results from cid_346, with that of the local LIRGs, there does not appear to be a significant evolution in the hot-to-cold molecular gas masses with redshift, at least until cosmic Noon. On the other hand, Dale et al. (2005) reported lower hot-to-cold gas mass ratios of $\sim 10^{-7} - 10^{-5}$ in a heterogenous sample of nearby galaxies, but predominantly normal star-forming galaxies. The lower hot-to-cold gas mass ratios in non-AGN galaxies may suggest that instead of a redshift evolution in the ratio, it may be the AGN luminosity that drives the hot molecular gas masses to higher values. However, more statistics are required at Cosmic Noon that includes both star-forming and AGN host galaxies to isolate the redshift evolution and AGN impact on molecular gas. Focusing only on the hot-to-cold gas ratio of cid_346, our results from JWST/MRS spectroscopy, therefore, suggest that at cosmic noon, the bulk of the molecular gas still exists in the cold gas phase. When comparing the mass of total molecular gas in AGN versus non-AGN host galaxies after taking into account the hot molecular gas mass, we would still end up with a systematic difference in the molecular gas content between the two classes of galaxies. On the other hand, as mentioned earlier in this section, the findings in this paper reveals that the impact of the AGN on molecular gas may be observed on localised spatial scales. Future *JWST*/MRS observations of both AGN and star-forming galaxies at cosmic noon are required to expand our measurements of the relative amount of hot and cold molecular gas phases and the detectability of the warm gas phase in a general population of galaxies at that epoch. An MRS+ALMA study of a statistical sample of galaxies will also reveal if there are systematic differences in the hot molecular gas properties between mass-matched AGN and star-forming galaxies, as is revealed with ALMA for the cold gas phase (e.g. Kakkad et al. 2017; Circosta et al. 2021; Bertola et al. 2024).

PSF-subtracted NIRCam images of cid_346 from COSMOS-Web survey reveals the presence of at least two companions roughly towards the south east of the AGN location. This may explain the presence of extended multiphase gas reservoir in this system, although the exact locations of the continua may not correspond to the locations of the spatial peaks or clumps of the extended gas, as shown in the right panel of Fig. 10. The indications of satellite galaxies

may suggest a merger-driven growth of both the supermassive black hole as well as star formation in the host galaxy of cid_346. At the same time, the accretion appears to drive multiphase outflows, clearly seen in the [O III]-based ionised gas and tentative indications in the hot molecular gas. However, we make a few observations about the outflows in different gas phases: First: In ground-based IFS data, it is possible that red-shifted and blue-shifted components of the emission lines (from the inflow or outflow or simply due to turbulence in the merger) got blended with each other, which may artificially broadened emission lines. Second: The absence of wings in molecular gas tracers compared to ionised gas could be due to the fact that molecular gas might be dominated by emission from the disc of the host galaxy, while the [O III]emission may be dominated by emission from the NLR. At low-redshift, for example in the interacting system Arp 220 (see Perna et al. 2024), wings representing outflowing gas has been observed in Pa-α or iron lines (Fe II), but such broad line profiles are not detected in the H_2 transitions, similar the observations here (see also Speranza et al. 2022). On the other hand, limited SNR or the limited spectral resolution in the H_2 spectra may also limit the detection rates of outflow wings underneath the lines. Therefore, future deeper MRS observations of this source are required to reveal potential wings in the individual emission line profiles and diffuse hot molecular gas emission around the cid_346 system.

6 CONCLUSIONS AND FINAL REMARKS

We analysed MIRI/MRS spectra and NIRCam images of an AGN host galaxy at Cosmic noon, cid_346. Previous ground-based spatially resolved observational campaigns of cid_346 already showed the presence of extended outflowing ionised gas with a large reservoir of cold molecular gas. The primary aim of the MRS spectroscopy was to search for the hot molecular gas phase using the ro-vibrational transitions in the rest-frame near-infrared spectra such as the 1–0 S(1) transition at 2.12 μm. The following summarizes the findings presented in this paper:

(i) We detect ro-vibrational transition of the H_2 molecule, particularly the 1–0 S(1) and 1–0 S(0) lines. The molecular lines are likely excited by X-ray heating from the AGN. We find an excitation temperature of 1100^{+465}_{-245} K and a total hot molecular gas of $\sim 8.0 \times 10^5 M_\odot$. The hot molecular gas mass is nearly five to six orders of magnitude less than ALMA CO-based cold gas mass, similar to hot-to-cold molecular gas mass ratios observed at low-redshift. This suggests that cold molecular gas dominates the bulk of the molecular gas budget in this galaxy and that the hot-to-cold molecular gas ratio does not appear to change with redshift.

(ii) We find extended hot molecular gas towards the SE of the AGN location up to a distance of 2.0 arcsec (∼16 kpc). The extended emission is roughly in the same direction as the extended ionized gas observed in ground-based IFS observations. A re-analysis of ALMA data also revealed extended CO(3–2) emission at $\sim 3\sigma$ level. Nearly 60 per cent of hot molecular gas is in the central AGN host, cid_346 and the rest in extended regions. In the case of cold molecular gas, 80 per cent is in the central AGN host and 20 per cent in the extended regions. Comparing the H_2 2.12 μm emission with VLA A-array 6.2 GHz radio emission suggests that the extended ro-vibrational transitions may be excited by the radio jets.

(iii) NIRCam imaging reveals the presence of two satellite galaxies near cid_346. Photometric and SED fitting analysis suggests that the stellar mass of these satellites is ∼100 times lower than that of the central AGN host galaxy, cid_346. Collectively, the cid_346 system is abundant with multi-phase gas, extended to tens of kiloparsec scales from the central AGN location.

The results presented in this paper showcases the capability of *JWST* mid-infrared spectrographs to detect hot molecular gas in galaxies at Cosmic noon. Future surveys targeting a statistical sample of both AGN and star-forming galaxies will be essential to derive a multiphase molecular gas picture at an epoch where feedback from AGN and/or star formation is expected to play a pivotal role. Additionally, deep resolved observations with both *JWST* and ALMA are required to understand the origins of the extended multiphase molecular gas. Furthermore, comparison with zoom-in simulations on the impact of radiation on molecular gas composition will be crucial to infer the impact of AGN on preventative mode feedback by heating molecular gas to higher temperatures.

ACKNOWLEDGEMENTS

We thank the anonymous referee for their constructive comments and suggestions. This work used the CANDIDE computer system at the Institut d'Astrophysique de Paris, which was funded through grants from the PNCG, CNES, DIM-ACAV, and the Cosmic Dawn Center and maintained by S. Rouberol. Numerical computations were in part carried out on the iDark cluster, Kavli IPMU. Kavli IPMU was supported by World Premier International Research Center Initiative (WPI), MEXT, Japan. TT was supported by JSPS KAKENHI Grant Number 25KJ0750 and the Forefront Physics and Mathematics Program to Drive Transformation (FoPM), a World-leading Innovative Graduate Study (WINGS) Program at the University of Tokyo. EB and GC acknowledge financial support from INAF under the Large Grant 2022 'The metal circle: a new sharp view of the baryon cycle up to Cosmic Dawn with the latest generation IFU facilities'. GSI acknowledges financial support from the Fundação de Amparo à Pesquisa do Estado de São Paulo (FAPESP), under Projects 2022/11799-9 and 2024/02487-9. SC acknowledges support by European Union's HE ERC Starting Grant No. 101040227—WINGS. MP acknowledges grant PID2021-127718NB-I00 funded by the Spanish Ministry of Science and Innovation/State Agency of Research (MICIN/AEI/10.13039/501100011033), and the grant RYC2023-044853-I, funded by MICIU/AEI/10.13039/501100011033 and European Social Fund Plus (FSE +). RAR acknowledges the support from Conselho Nacional de Desenvolvimento Científico e Tecnológico (CNPq; Proj. 303450/2022-3, 403398/2023-1, & 441722/2023-7), Fundação de Amparo à pesquisa do Estado do Rio Grande do Sul (FAPERGS; Proj. 21/2551-0002018-0), and Coordenação de Aperfeiçoamento de Pessoal de Nível Superior (CAPES; Proj. 88887.894973/2023-00). GT acknowledges financial support from the European Research Council (ERC) Advanced Grant under the European Union's Horizon Europe research and innovation programme (grant agreement AdG GALPHYS, No. 101055023). IL acknowledges support from PRIN-MUR project 'PROMETEUS' financed by the European Union—Next Generation EU, Mission 4 Component 1 CUP B53D23004750006. CMH acknowledges funding from an United Kingdom Research and Innovation grant (code: MR/V022830/1). This paper makes use of the following ALMA data: ADS/JAO.ALMA#2016.1.00798.S. ALMA is a partnership of ESO (representing its member states), NSF (USA) and NINS (Japan), together with NRC (Canada), NSC and ASIAA (Taiwan), and KASI (Republic of Korea), in cooperation with the Republic of Chile. The Joint ALMA Observatory is operated by ESO, AUI/NRAO and NAOJ. This work is based [in part] on observations made with the NASA/ESA/CSA James Webb Space Telescope. The

data were obtained from the Mikulski Archive for Space Telescopes at the Space Telescope Science Institute, which is operated by the Association of Universities for Research in Astronomy, Inc., under NASA contract NAS 5-03127 for JWST. These observations are associated with program 2177.

DATA AVAILABILITY

The data used in this paper is available in the MAST portal of STScI and in ESO and ALMA archives.

REFERENCES

Armus L. et al., 2023, ApJ, 942, L37
Arribas S., Colina L., Bellocchi E., Maiolino R., Villar-Martín M., 2014, A&A, 568, A14
Baldwin J. A., Phillips M. M., Terlevich R., 1981, PASP, 93, 5
Barfety C. et al., 2025, ApJ, 988, 55
Benson A. J., Bower R. G., Frenk C. S., Lacey C. G., Baugh C. M., Cole S., 2003, ApJ, 599, 38
Bertin E., 2011, in Evans I. N., Accomazzi A., Mink D. J., Rots A. H., eds, ASP Conf. Ser., Vol. 442, Astronomical Data Analysis Software and Systems XX. Astron. Soc. Pac., San Francisco, p. 435
Bertin E., Arnouts S., 1996, A&AS, 117, 393
Bertola E. et al., 2024, MNRAS, 691, 178
Bessiere P. S., Ramos Almeida C., 2022, MNRAS, 512, L54
Birkin J. E. et al., 2021, MNRAS, 501, 3926
Bischetti M. et al., 2021, A&A, 645, A33
Black J. H., van Dishoeck E. F., 1987, ApJ, 322, 412
Boogaard L. A. et al., 2020, ApJ, 902, 109
Boquien M., Burgarella D., Roehlly Y., Buat V., Ciesla L., Corre D., Inoue A. K., Salas H., 2019, A&A, 622, A103
Brusa M. et al., 2018, A&A, 612, A29
Bruzual G., Charlot S., 2003, MNRAS, 344, 1000
Bushouse H. et al., 2024, JWST Calibration Pipeline, Zenodo: https://doi.org/10.5281/zenodo.15880261
Calzetti D., 2013, in Falcón-Barroso J., Knapen J. H., eds, Secular Evolution of Galaxies. p. 419, https://ui.adsabs.harvard.edu/abs/2013seg
Calzetti D., Armus L., Bohlin R. C., Kinney A. L., Koornneef J., Storchi-Bergmann T., 2000, ApJ, 533, 682
Cano-Díaz M., Maiolino R., Marconi A., Netzer H., Shemmer O., Cresci G., 2012, A&A, 537, L8
Carilli C. L., Walter F., 2013, ARA&A, 51, 105
Carniani S. et al., 2015, A&A, 580, A102
Carniani S. et al., 2016, A&A, 591, A28
Carniani S. et al., 2023, A&A, 685, A99
Casey C. M. et al., 2023, ApJ, 954, 31
Chabrier G., 2003, PASP, 115, 763
Chen Y.-C. et al., 2024, ApJ, 968, 92
Cicone C. et al., 2014, A&A, 562, A21
Cicone C. et al., 2021, A&A, 654, L8
Circosta C. et al., 2018, A&A, 620, A82
Circosta C. et al., 2021, A&A, 646, A96
Civano F. et al., 2016, ApJ, 819, 62
Cresci G. et al., 2015, ApJ, 799, 82
Dale D. A., Sheth K., Helou G., Regan M. W., Hüttemeister S., 2005, AJ, 129, 2197
Dasyra K. M., Combes F., 2011, A&A, 533, L10
Davé R., Anglés-Alcázar D., Narayanan D., Li Q., Rafieferantsoa M. H., Appleby S., 2019, MNRAS, 486, 2827
Davies R. et al., 2020, MNRAS, 498, 4150
Davies R. et al., 2024, A&A, 689, A263
Davies R. I., Maciejewski W., Hicks E. K. S., Tacconi L. J., Genzel R., Engel H., 2009, ApJ, 702, 114
Ding X. et al., 2020, ApJ, 888, 37
Dubois Y., Peirani S., Pichon C., Devriendt J., Gavazzi R., Welker C., Volonteri M., 2016, MNRAS, 463, 3948
Ellison S. L. et al., 2021, MNRAS, 505, L46
Elmegreen B. G., 1989, ApJ, 338, 178
Emonts B. H. C., Colina L., Piqueras-López J., Garcia-Burillo S., Pereira-Santaella M., Arribas S., Labiano A., Alonso-Herrero A., 2017, A&A, 607, A116
Esparza-Arredondo D. et al., 2025, A&A, 693, A174
Fabian A. C., 2012, ARA&A, 50, 455
Fabian A. C., Vasudevan R. V., Gandhi P., 2008, MNRAS, 385, L43
Fiore F. et al., 2017, A&A, 601, A143
Fluetsch A. et al., 2019, MNRAS, 483, 4586
Förster Schreiber N. M. et al., 2018, ApJS, 238, 21
Frias Castillo M. et al., 2024, A&A, 683, A211
Friedrich S., Davies R. I., Hicks E. K. S., Engel H., Müller-Sánchez F., Genzel R., Tacconi L. J., 2010, A&A, 519, A79
García-Burillo S. et al., 2024, A&A, 689, A347
Genel S. et al., 2014, MNRAS, 445, 175
Glazebrook K., Blake C., Economou F., Lilly S., Colless M., 1999, MNRAS, 306, 843
Harrison C. M., 2017, Nat. Astron., 1, 0165
Harrison C. M., Alexander D. M., Mullaney J. R., Swinbank A. M., 2014, MNRAS, 441, 3306
Hernandez S. et al., 2023, ApJ, 948, 124
Hirschmann M. et al., 2023, MNRAS, 526, 3610
Hirschmann M., De Lucia G., Wilman D., Weinmann S., Iovino A., Cucciati O., Zibetti S., Villalobos Á., 2014, MNRAS, 444, 2938
Hollenbach D., McKee C. F., 1989, ApJ, 342, 306
Husemann B., Davis T. A., Jahnke K., Dannerbauer H., Urrutia T., Hodge J., 2017, MNRAS, 470, 1570
Jin S. et al., 2018, ApJ, 864, 56
Jones G. C., Maiolino R., Circosta C., Scholtz J., Carniani S., Fudamoto Y., 2023, MNRAS, 518, 691
Kakkad D. et al., 2016, A&A, 592, A148
Kakkad D. et al., 2017, MNRAS, 468, 4205
Kakkad D. et al., 2020, A&A, 642, A147
Kakkad D. et al., 2022, MNRAS, 511, 2105
Kakkad D. et al., 2023b, MNRAS, 520, 5783
Kakkad D., Stalevski M., Kishimoto M., Knežević S., Asmus D., Vogt F. P. A., 2023a, MNRAS, 519, 5324
Kauffmann G. et al., 2003, MNRAS, 346, 1055
Kennicutt R. C., Jr, 1998, ARA&A, 36, 189
Kennicutt R. C., Evans N. J., 2012, ARA&A, 50, 531
Kewley L. J., Dopita M. A., Sutherland R. S., Heisler C. A., Trevena J., 2001, ApJ, 556, 121
Kirkpatrick A., Sharon C., Keller E., Pope A., 2019, ApJ, 879, 41
Koekemoer A. M. et al., 2007, ApJS, 172, 196
Koss M. et al., 2017, ApJ, 850, 74
Koss M. J. et al., 2021, ApJS, 252, 29
Labiano A. et al., 2016, in Peck A. B., Seaman R. L., Benn C. R., eds, SPIE Conf. Ser., Vol. 9910, Observatory Operations: Strategies, Processes, and Systems VI. SPIE, Bellingham, p. 99102W
Lamperti I. et al., 2017, MNRAS, 467, 540
Law D. R., E. Morrison J., Argyriou I., Patapis P., Álvarez-Márquez J., Labiano A., Vandenbussche B., 2023, AJ, 166, 45
Loiacono F. et al., 2024, A&A, 685, A121
Lutz D. et al., 2020, A&A, 633, A134
Madau P., Dickinson M., 2014, ARA&A, 52, 415
Mainieri V. et al., 2021, The Messenger, 182, 45
Maloney P. R., Hollenbach D. J., Tielens A. G. G. M., 1996, ApJ, 466, 561
McNamara B. R., Nulsen P. E. J., 2007, ARA&A, 45, 117
Mercedes-Feliz J. et al., 2024, MNRAS, 530, 2795
Mezcua M., Pacucci F., Suh H., Siudek M., Natarajan P., 2024, ApJ, 966, L30
Mouri H., 1994, ApJ, 427, 777
Murphy E. J. et al., 2011, ApJ, 737, 67
Nelson D. et al., 2019, Comput. Astrophys. Cosmol., 6, 2
Oke J. B., 1974, ApJS, 27, 21
Padovani P. et al., 2017, A&A Rev., 25, 2
Pereira-Santaella M. et al., 2016, A&A, 594, A81
Perna M. et al., 2024, A&A, 690, A171

Pillepich A. et al., 2018, MNRAS, 473, 4077
Rakshit S., Woo J.-H., 2018, ApJ, 865, 5
Ramos Almeida C., Ricci C., 2017, Nat. Astron., 1, 679
Reines A. E., Volonteri M., 2015, ApJ, 813, 82
Rennehan D., Babul A., Moa B., Davé R., 2024, MNRAS, 532, 4793
Reunanen J., Kotilainen J. K., Prieto M. A., 2002, MNRAS, 331, 154
Ricci C. et al., 2017, Nature, 549, 488
Rieke M. J. et al., 2023, PASP, 135, 028001
Riffel R. A. et al., 2023, MNRAS, 521, 1832
Riffel R. A., Bianchin M., Riffel R., Storchi-Bergmann T., Schönell A. J., Dahmer-Hahn L. G., Dametto N. Z., Diniz M. R., 2021, MNRAS, 503, 5161
Riffel R. A., Storchi-Bergmann T., Winge C., McGregor P. J., Beck T., Schmitt H., 2008, MNRAS, 385, 1129
Riffel R., Rodríguez-Ardila A., Pastoriza M. G., 2006, A&A, 457, 61
Rodríguez-Ardila A., Riffel R., Pastoriza M. G., 2005, MNRAS, 364, 1041
Rosario D. J. et al., 2012, A&A, 545, A45
Rosario D. J. et al., 2018, MNRAS, 473, 5658
Rosario D. J., Togi A., Burtscher L., Davies R. I., Shimizu T. T., Lutz D., 2019, ApJ, 875, L8
Roueff E., Abgrall H., Czachorowski P., Pachucki K., Puchalski M., Komasa J., 2019, A&A, 630, A58
Roy N. et al., 2024, ApJ, 970, 69
Rupke D. S. N., Veilleux S., 2013, ApJ, 768, 75
Saintonge A., Catinella B., 2022, ARA&A, 60, 319
Schawinski K., Koss M., Berney S., Sartori L. F., 2015, MNRAS, 451, 2517
Schaye J. et al., 2015, MNRAS, 446, 521
Schaye J. et al., 2023, MNRAS, 526, 4978
Schreiber C. et al., 2015, A&A, 575, A74
Schwarz G., 1978, Ann. Stat., 6, 461
Scoville N. et al., 2007, ApJS, 172, 1
Shankar F., Weinberg D. H., Miralda-Escudé J., 2009, ApJ, 690, 20
Silk J., Mamon G. A., 2012, Res. Astron. Astrophys., 12, 917
Somerville R. S., Hopkins P. F., Cox T. J., Robertson B. E., Hernquist L., 2008, MNRAS, 391, 481
Speranza G. et al., 2022, A&A, 665, A55
Storchi-Bergmann T., McGregor P. J., Riffel R. A., Simões Lopes R., Beck T., Dopita M., 2009, MNRAS, 394, 1148
Tacchella S. et al., 2022, MNRAS, 513, 2904
Tacconi L. J. et al., 2018, ApJ, 853, 179
Tanaka T. S. et al., 2024, ApJ, 979, 215
Tozzi G. et al., 2024, A&A, 690, A141
Travascio A. et al., 2024, A&A, 686, A250
Turner J., Kirby-Docken K., Dalgarno A., 1977, ApJS, 35, 281
Übler H. et al., 2023, A&A, 677, A145
Ulivi L. et al., 2025, A&A, 693, A36
Vanden Berk D. E. et al., 2001, AJ, 122, 549
Vayner A. et al., 2024, ApJ, 960, 126
Veilleux S., Maiolino R., Bolatto A. D., Aalto S., 2020, A&AR, 28, 2
Vietri G. et al., 2020, A&A, 644, A175
Ward S. R., Costa T., Harrison C. M., Mainieri V., 2024, MNRAS, 533, 1733
Ward S. R., Harrison C. M., Costa T., Mainieri V., 2022, MNRAS, 514, 2936
Weaver J. R. et al., 2022, ApJS, 258, 11
Wilman R. J., Edge A. C., Johnstone R. M., 2005, MNRAS, 359, 755
Wolniewicz L., Simbotin I., Dalgarno A., 1998, ApJS, 115, 293
Wylezalek D., Flores A. M., Zakamska N. L., Greene J. E., Riffel R. A., 2020, MNRAS, 492, 4680
Yang G. et al., 2022, ApJ, 927, 192
Zuther J., Iserlohe C., Pott J. U., Bertram T., Fischer S., Voges W., Hasinger G., Eckart A., 2007, A&A, 466, 451

APPENDIX A: EXTRA MATERIAL

[1]*Centre for Astrophysics Research, Department of Physics, Astronomy and Mathematics, University of Hertfordshire, Hatfield, AL10 9AB, UK*
[2]*Space Telescope Science Institute, 3700 San Martin Drive, Baltimore, MD 21218, USA*

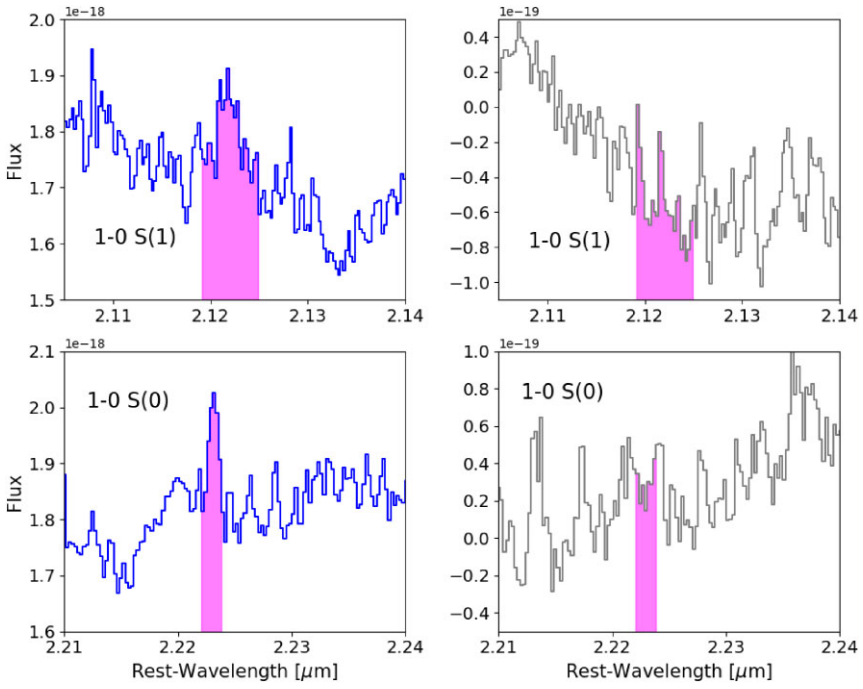

Figure A1. Comparison of H_2 detections in cid_346 integrated spectra (blue curves in the left panels) with spectra extracted from object-free regions (grey curve in the right panel). The magenta shaded regions mark the location of the 1–0 S(1) and 1–0 S(0) lines in the top and bottom panels, respectively.

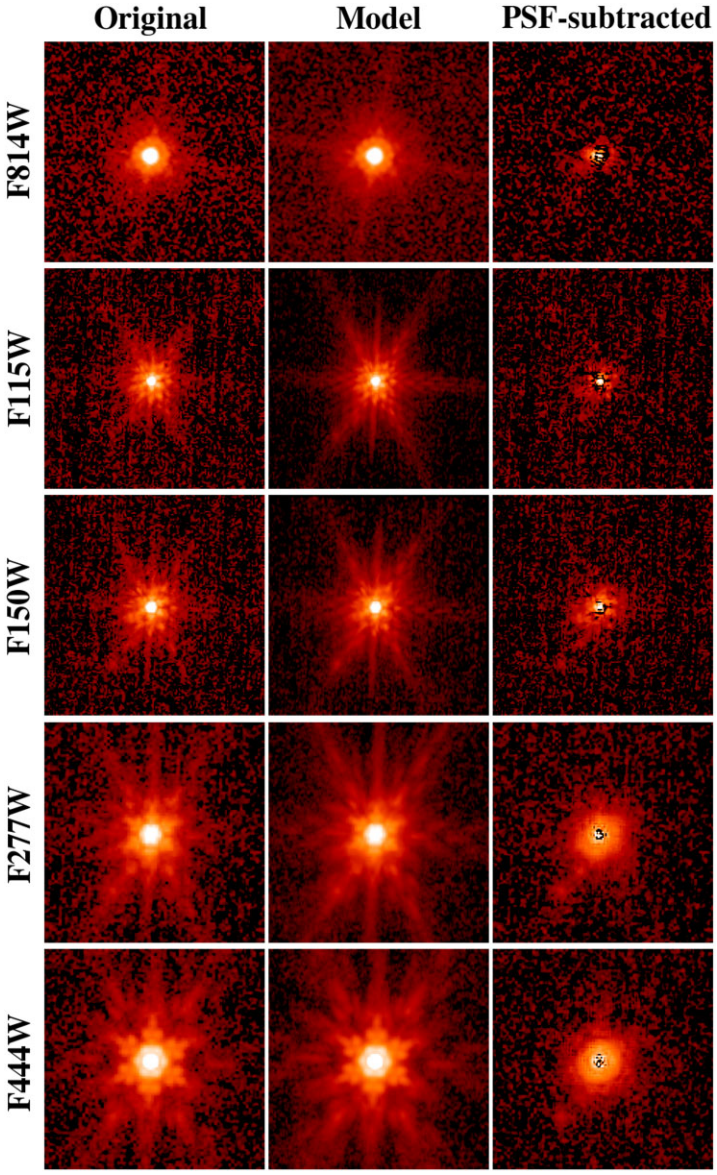

Figure A2. This figure shows the NIRCam images from all the observed filters covered in COSMOS-Web campaign. Left panels show the original image, the middle panel shows the image models (see Section 4.3) and the right panel shows the residuals after subtracting the models in the middle panel from the original images in the left panel. The presence of two extended companions is clear, especially in the PSF-subtracted images from the filters F150W, F277W, and F444W.

[3]*European Southern Observatory, Karl-Schwarzschild-Strasse 2, 85748 Garching bei München, Germany*
[4]*Department of Astronomy, Graduate School of Science, The University of Tokyo, 7-3-1 Hongo, Bunkyo-ku, Tokyo 113-0033, Japan*
[5]*Kavli Institute for the Physics and Mathematics of the Universe (WPI), The University of Tokyo Institutes for Advanced Study, Kashiwa, Chiba 277-8583, Japan*
[6]*Center for Data-Driven Discovery, Kavli IPMU (WPI), UTIAS, The University of Tokyo, Kashiwa, Chiba 277-8583, Japan*
[7]*Center for Astrophysical Sciences, Department of Physics & Astronomy, Johns Hopkins University, Baltimore, MD 21218, USA*
[8]*Departamento de Física/CCNE, Universidade Federal de Santa Maria, 97105-900 Santa Maria, RS, Brazil*
[9]*ESA, European Space Astronomy Centre (ESAC), Camino Bajo del Castillo s/n, E-28692 Villanueva de la Cañada, Madrid, Spain*
[10]*Institut de Radioastronomie Millimétrique (IRAM), 300 rue de la Piscine, 38400 Saint-Martin-d'Hères, France*
[11]*INAF-Osservatorio Astrofisico di Arcetri, Largo E. Fermi 5, I-50125 Firenze, Italy*
[12]*Department of Physics and Astronomy, 4129 Frederick Reines Hall, University of California, Irvine, CA 92697, USA*
[13]*Dipartimento di Fisica, Universitá di Trieste, Sezione di Astronomia, Via G.B. Tiepolo 11, I-34131 Trieste, Italy*
[14]*INAF–Osservatorio Astronomico di Trieste, Via G. B. Tiepolo 11, I–34131 Trieste, Italy*
[15]*German Aerospace Center (DLR), Institute of Communications and Navigation, 82234 Wessling, Germany*
[16]*Scuola Normale Superiore, Piazza dei Cavalieri 7, I-56126 Pisa, Italy*
[17]*Institute of Theoretical Astrophysics, University of Oslo, PO Box 1029, Blindern, 0315 Oslo, Norway*
[18]*INAF–Osservatorio Astrofisico di Arcetri, Largo E. Fermi 5, I-50125 Florence, Italy*
[19]*School of Mathematics, Statistics and Physics, Newcastle University, Newcastle upon Tyne, NE1 7RU, UK*

[20]*Dipartimento di Fisica e Astronomia, Università di Firenze, Via G. Sansone 1, I-50019 Sesto F.no (Firenze), Italy*
[21]*Kavli Institute for Astronomy and Astrophysics, Peking University, Beijing 100871, People's Republic of China*
[22]*Kavli IPMU (WPI), UTIAS, The University of Tokyo, Kashiwa, Chiba 277-8583, Japan*
[23]*Centre for Data-Driven Discovery, Kavli IPMU (WPI), UTIAS, The University of Tokyo, Kashiwa, Chiba 277-8583, Japan*
[24]*Centro de Astrobiología (CAB), CSIC–INTA, Cra. de Ajalvir Km. 4, 28850–Torrejón de Ardoz, Madrid, Spain*
[25]*INAF–Osservatorio Astronomico di Roma, Via Frascati 33, I-00040 Monte Porzio Catone, Italy*
[26]*School of Physics and Astronomy, University of Southampton, Highfield SO17 1BJ, UK*
[27]*Universidade de São Paulo, Instituto de Astronomia, Geofísica e Ciências Atmosféricas, Rua do Matão 1226, CEP 05508-090 São Paulo, SP, Brazil*
[28]*Max-Planck-Institut für Extraterrestrische Physik (MPE), Giessenbachstraße 1, D-85748 Garching, Germany*
[29]*INAF–Istituto di Astrofisica Spaziale e Fisica cosmica Milano, Via Alfonso Corti 12, 20133 Milano, Italy*
[30]*Dipartimento di Fisica e Astronomia 'Augusto Righi', Universitá degli Studi di Bologna, via P. Gobetti, 93/2, 40129 Bologna, Italy*
[31]*INAF–Osservatorio di Astrofisica e Scienza dello Spazio di Bologna, via Piero Gobetti, 93/3, I-40129 Bologna, Italy*
[32]*Center for Computational Astrophysics, Flatiron Institute, 162 Fifth Avenue, New York, NY 10010, USA*

This paper has been typeset from a TEX/LATEX file prepared by the author.